electronics

Article

A Novel Adaptive RNN-Based Control Strategy for Deep Flux-Weakening Operation of IPMSMs

Zhuang Yang, Wanlu Zhu * and Pengfei Zhi

School of Automation, Jiangsu University of Science and Technology, Changshan Campus, Zhenjiang 212100, China; yangzhuang@stu.just.edu.cn (Z.Y.); zhipengfei@just.edu.cn (P.Z.)
* Correspondence: zhuwanlu@just.edu.cn

Abstract

For the deep flux-weakening speed regulation of interior permanent magnet synchronous motors (IPMSMs), the conventional formula-based tuning method is highly complex. To address this issue, an IPMSM deep flux-weakening control strategy based on an adaptive RNN is proposed. This paper first analyzes traditional deep flux-weakening methods for permanent magnet synchronous motors. Building upon deep flux-weakening control, an adaptive RNN is integrated with the maximum torque per voltage (MTPV) strategy in the deep flux-weakening region. The neural network model is constructed with the input layer comprising the d-axis and q-axis currents from the previous time step, the current motor speed, and the target reference speed, while the output layer provides the required d-axis and q-axis currents for the control system at the current time step. Finally, the algorithm is implemented and validated through a simulation model built in MATLABR2024b/SIMULINK. The simulation results demonstrate that the proposed adaptive RNN-based IPMSM deep flux-weakening control system exhibits improved accuracy and robustness.

Keywords: IPMSM; flux-weakening control; RNN; deep flux-weakening operation

check for updates

Academic Editor: Yang-Ki Hong

Received: 19 November 2025
Revised: 11 December 2025
Accepted: 15 December 2025
Published: 16 December 2025

Citation: Yang, Z.; Zhu, W.; Zhi, P. A Novel Adaptive RNN-Based Control Strategy for Deep Flux-Weakening Operation of IPMSMs. *Electronics* **2025**, *14*, 4934. https://doi.org/10.3390/electronics14244934

Copyright: © 2025 by the authors. Licensee MDPI, Basel, Switzerland. This article is an open access article distributed under the terms and conditions of the Creative Commons Attribution (CC BY) license (https://creativecommons.org/licenses/by/4.0/).

1. Introduction

With the development of new energy vehicles, inverter air conditioners, washing machines, and other fields, as well as the increasing demand for stable high-speed operation of motors, flux-weakening speed regulation of permanent magnet synchronous motors (PMSM) is becoming a research hotspot in the field of motor speed control [1]. In the research area of PMSM speed regulation, flux-weakening region quadrant switching technology and deep flux-weakening technology are currently the two most important aspects [2]. The significance of these technologies lies in ensuring that the PMSM can operate stably with anti-interference capability under high torque and complex speed regulation conditions without losing control, thereby improving the reliability of flux-weakening control and achieving flexible speed regulation across the entire speed range of the PMSM [3,4]. Among the structural types of PMSMs, compared to surface-mounted permanent magnet synchronous motors, the interior permanent magnet synchronous motor (IPMSM) embeds the permanent magnets inside the rotor, and its magnetic circuit structure exhibits reluctance differences, making it easier to achieve flux-weakening control [5]. Therefore, research on IPMSM flux-weakening control holds significant theoretical and practical application value [6]. In terms of theoretical significance, with the increasing maturity of intelligent algorithms, integrating them with classical motor control methods such as direct torque control and vector control enables the intelligent and high-performance enhancement of motor control strategies [7,8]. In practical applications, the research outcomes of motor flux-weakening control can be widely applied to significantly improve motor operating efficiency, reduce motor losses, and to some extent lower economic costs, aligning with the principles of green environmental protection and energy saving in the new era [9–11]. In summary, research on IPMSM flux-weakening control technology not only meets the modern industrial demand for high-performance and high-efficiency motors but also provides important support for the innovation and application expansion of motor drive technology, possessing broad theoretical value and practical significance.

Flux-weakening control, as a core technology enabling permanent magnet synchronous motors to achieve high-speed operation, demonstrates significant advantages in broadening the speed regulation range and enhancing operational efficiency. However, its engineering application faces complex technical challenges [2,10]. This technology exhibits a strong dependence on motor parameters, which are prone to nonlinear drift during operation due to factors like magnetic saturation and temperature variation. Furthermore, the cross-coupling effect between the d-axis and q-axis magnetic circuits intensifies this nonlinear parameter behavior [12]. Magnetic saturation and cross-saturation phenomena can significantly alter inductance parameters, thereby adversely affecting the accuracy of motor torque output. Regarding dynamic response characteristics, issues such as oscillatory step response exist, and the insufficient precision of dynamic models struggles to meet the demands of high-performance control [13–15]. From the perspective of hardware implementation, flux-weakening control is constrained by the voltage output range of the inverter. Simultaneously, high-precision control strategies often entail complex computational processes, leading to a significant increase in system costs [16]. Additionally, the system confronts the challenge of electromagnetic-thermal-mechanical multi-physics coupling. The complexity of the interaction mechanisms among these multiple physical fields further escalates the difficulty of system design and optimization [17–19].

To meet the requirement for a wide speed regulation range in IPMSMs, flux-weakening control is implemented by sacrificing part of the motor's load-bearing capacity while ensuring the driving torque meets the demand. IPMSM flux-weakening control is generally achieved by increasing the d-axis current, with various commonly used implementation methods. Among them, the formula-based method, look-up table method, gradient descent method, and advanced angle flux-weakening method are considered classic approaches [20–22].

The formula-based method relies on rigorous theoretical derivation and mathematical modeling. It features clear logic, directly defining the conditions for IPMSM flux-weakening speed regulation and its constraint relationship with the DC bus voltage. Consequently, it can precisely determine a reasonable d-axis current value for the current operating condition while ensuring system stability. However, its performance depends on the accuracy of motor parameters and demands high computational power from the motor control chip, making its development constrained by hardware conditions [23,24].

The look-up table method is often applied in the flux-weakening tuning of IPMSMs for electric vehicles. It requires extensive experimental data for offline tuning to avoid complex online calculations. Since its flux-weakening rules are successfully tuned before motor operation, it can significantly reduce the online computational burden on the controller. Nevertheless, its drawbacks are quite evident: it is highly dependent on motor parameters, and the algorithm has poor portability, requiring re-tuning for flux-weakening speed regulation of different motor models [25,26].

The gradient descent method is a numerical solution that iteratively searches for the optimal solution based on information from an objective function. It adjusts parameters step-by-step in the direction of the fastest decrease in the function value until convergence meets the stopping criteria or reaches its minimum value, with its core being optimization. It does not rely on a highly precise motor model, offering significant advantages in scenarios where IPMSM parameters are unknown or prone to change. The shortcomings of the gradient descent method are also apparent: it is susceptible to the influence of the given initial value, potentially causing the IPMSM to fall into local optima and resulting in insufficient flux-weakening depth. It proves effective in low-speed, high-precision motor control, but requires strategy optimization for high-power, high-speed motors subjected to significant disturbances [27].

In the exploration of achieving high-performance speed control for permanent magnet synchronous motors, the evolution of control strategies has consistently focused on balancing dynamic response speed, steady-state accuracy, and robustness under conditions of nonlinearity, time-varying parameters, and unknown disturbances. Early research primarily relied on classical linear control theory, whose performance was limited by the requirement for precise mathematical models. In recent years, advanced control theories represented by fuzzy logic, fractional-order calculus, and sliding mode variable structure have provided new avenues for resolving these conflicts. For instance, the "Fuzzy Adaptive Fractional-order Pulse Width Modulation based on Torque Compensation" method proposed in reference [28] makes its core contribution by integrating the fine-tuning capability of fractional-order systems with the online adaptive ability of fuzzy systems. It compensates for torque ripple in a feedforward manner, thereby achieving significant improvements in both steady-state accuracy and dynamic smoothness. Parallel to this, another developmental path focuses on enhancing system convergence speed and robustness. As seen in the "Adaptive Fractional-order Fast Terminal Sliding Mode Control" proposed in reference [29], it constructs a fractional-order fast terminal sliding surface and designs an adaptive law to estimate the upper bound of disturbances online. This effectively ensures the finite-time convergence of system states and significantly suppresses chattering. These works advance the development of high-performance control from two distinct dimensions: "precision suppression" and "strong disturbance rejection," respectively.

To address the aforementioned issues of difficult linear tuning in traditional deep flux-weakening controllers and the potential risk of system instability, this paper proposes a composite control strategy that combines fast, finite-time convergence with strong robustness, while achieving high-precision adaptive regulation. Specifically, an IPMSM deep flux-weakening control method based on an adaptive RNN is introduced [30]. This approach not only overcomes the shortcomings of traditional PI controllers, such as slow response and low accuracy during motor flux-weakening, but also resolves the difficulty in tuning output currents in deep flux-weakening operations.

The main contributions of this paper can be summarized into the following three points:

A novel method that integrates an adaptive recurrent neural network with deep flux-weakening control is proposed to overcome the issues of reliance on precise models and complex parameter tuning in traditional formula-based flux-weakening control, thereby significantly enhancing the system's dynamic response speed and anti-interference performance.

The structure of the traditional RNN recurrent unit is improved to enhance its ability to model long-term temporal dynamics during motor operation, effectively increasing the model's fitting accuracy and control robustness for complex motor dynamic behaviors.

Through MATLABR2024b/Simulink simulations, the effectiveness and feasibility of the proposed adaptive RNN-based deep flux-weakening control strategy for interior permanent magnet synchronous motors are systematically validated.

The organization of this paper is structured as follows: Section 2 establishes the mathematical model of the IPMSM and analyzes the traditional formula-based deep flux-weakening control method and its limitations. Section 3 addresses the issues of complex tuning and poor adaptability in traditional methods by proposing a deep flux-weakening control strategy based on an adaptive RNN. Section 4 conducts simulation verification of the proposed strategy, demonstrating its accuracy and practicality in IPMSM flux-weakening control. Section 5 summarizes the simulation results and discusses future research directions.

2. Deep Flux-Weakening Control for Interior Permanent Magnet Synchronous Motors

2.1. IPMSM Modeling

The Interior Permanent Magnet Synchronous Motor is named for its permanent magnets being embedded within the rotor core [5]. Investigating the theory of flux-weakening control for IPMSM and establishing an idealized mathematical model for this nonlinear, strongly coupled system is a crucial step in the analysis of its control strategies. The IPMSM model in the rotating reference frame is typically developed under idealized assumptions [31].

The voltage equations of the PMSM in the d-q reference frame are expressed as (1):

$$\begin{bmatrix} u_d \\ u_q \end{bmatrix} = \begin{bmatrix} R_s + \frac{dL_d}{dt} & -\omega_e L_q \\ \omega_e L_d & R_s + \frac{dL_q}{dt} \end{bmatrix} \begin{bmatrix} i_d \\ i_q \end{bmatrix} + \begin{bmatrix} 0 \\ \psi_f \omega_e \end{bmatrix} \tag{1}$$

where u_d, u_q denote the d- and q-axis stator voltages, respectively; i_d, i_q are the d- and q-axis currents; L_d, L_q represent the d- and q-axis inductances; ω_e is the electrical angular velocity; ψ_f is the permanent magnet flux linkage; and R_s is the stator resistance.

The flux linkage equations of the PMSM are expressed as (2):

$$\begin{bmatrix} \psi_d \\ \psi_q \end{bmatrix} = \begin{bmatrix} L_d \\ L_q \end{bmatrix} \begin{bmatrix} i_d & i_q \end{bmatrix} + \begin{bmatrix} \psi_f \\ 0 \end{bmatrix} \tag{2}$$

To reduce model complexity and considering that the motor operates at high speeds during flux-weakening, the effects of core loss and stator winding resistance are typically neglected.

The electromagnetic torque equation of the IPMSM is expressed as (3):

$$T_e = \frac{P_e}{\Omega} = \frac{3}{2} p_n (\psi_d i_q + \psi_q i_d) = \frac{3}{2} p_n \left[\psi_f i_q + (L_d - L_q) i_d i_q \right] \tag{3}$$

where Ω denotes the mechanical angular speed of the IPMSM, p_n is its number of pole pairs, $\psi_f i_q$ is the permanent magnet torque constant, and $(L_d - L_q) i_d i_q$ is the reluctance torque constant resulting from the IPMSM's saliency ratio.

The mechanical motion equation of the IPMSM is expressed as (4):

$$T_e - T_L = J \frac{d\Omega}{dt} + B\Omega \tag{4}$$

where T_L denotes the load torque, J is the moment of inertia, and B is the viscous friction coefficient.

2.2. Research on Deep Flux-Weakening in IPMSM

This subsection presents an in-depth study of the deep flux-weakening region in IPMSM. The characteristic current i_{ch} of the IPMSM is defined by Equation (5) as follows:

$$i_{ch} = -\frac{\psi_f}{L_d} \tag{5}$$

The saliency ratio Δ, the flux-weakening factor ρ, and the power factor $\cos\varphi$ of the IPMSM are defined by Equation (6) as follows:

$$\begin{cases} \Delta = \frac{L_q}{L_d} \\ \rho = \frac{L_d i_d}{\psi_f} \\ \cos\varphi = cos(\alpha - \beta) \end{cases} \tag{6}$$

here, Δ characterizes the relationship between the d- and q-axis inductances, ρ represents the flux-weakening capability of the IPMSM, and $\cos\varphi$ indicates the utilization capability of the inverter's DC-link voltage. The angle α is the angle by which the voltage vector leads the q-axis, and the angle β is the angle by which the current vector leads the q-axis.

In Figure 1, the curves labeled T_e represent constant torque curves. The Maximum Torque Per Ampere (MTPA) curve intersects the current limit circle at point A, which corresponds to the base speed ω_{basic} of the IPMSM. Point E represents the center of the voltage limit circle, and its corresponding d-axis current i_d is the characteristic current i_{ch}. The voltage limit circle is tangent to the current limit circle at point D, corresponding to the speed ω_D. As the speed of the IPMSM increases, the voltage limit ellipse begins to contract around point E. During the flux-weakening process, the operating trajectory is constrained by both the voltage and current limit circles, and the speed regulation region must lie within the constant torque zone, constant power zone, and deep flux-weakening zone [32].

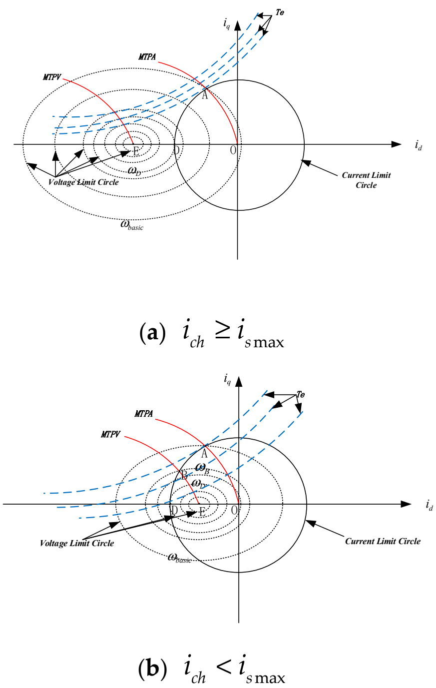

(**a**) $i_{ch} \geq i_{s\max}$

(**b**) $i_{ch} < i_{s\max}$

Figure 1. Analysis of the Deep Flux-Weakening Region.

As shown in Figure 1a, if $i_{ch} > i_{s\max}$, the theoretically maximum achievable speed of the IPMSM is ω_D. In this case, the Maximum Torque Per Voltage (MTPV) curve lies outside the feasible flux-weakening speed regulation region; hence, no deep flux-weakening zone exists. Forcibly switching to the MTPV curve would result in $i_d^2 + i_q^2 > i_{s\max}^2$, saturation of the current PI regulator, loss of control in the system, and potentially cause the IPMSM to overspeed (commonly referred to as "field-weakening runaway"). Similarly, if the motor operates in the critical condition where $i_{ch} = i_{\text{smax}}$, the deep flux-weakening region also does not exist.

As illustrated in Figure 1b, if $i_{ch} < i_{\text{smax}}$, the Maximum Torque Per Voltage (MTPV) curve intersects the current limit circle at point A. When the IPMSM accelerates from its base speed ω_{basic} and reaches point A—the intersection of the MTPV curve and the current limit circle—there exist numerous possible trajectories to approach the maximum speed point B. However, to achieve the maximum possible torque at any given speed within this range, flux-weakening speed regulation is performed along the MTPV trajectory. Consequently, point A serves as the boundary between the constant power region and the deep flux-weakening region.

Based on the preceding analysis, it can be concluded that the operating trajectory of the IPMSM within the deep flux-weakening region follows the MTPV curve. Under the MTPV condition, the expressions relating the d-axis current i_d and the q-axis current i_q to the electrical angular speed ω_e are given by Equation (7):

$$\begin{cases} i_d = -\frac{\psi_f}{L_d} + \frac{-L_q\psi_f + \sqrt{L_q^2\psi_f^2 + 8\left(L_d - L_q\right)^2\left(\frac{u_{\text{smax}}}{\omega_e}\right)^2}}{4\left(L_d - L_q\right)L_d} = -\frac{\psi_f}{L_d} + \Delta i_d \\ i_q = \frac{\sqrt{\left(\frac{u_{\text{smax}}}{\omega_e}\right)^2 - L_d^2\Delta i_d^2}}{L_q} \end{cases} \tag{7}$$

where $\Delta i_d = \frac{-L_q\psi_f + \sqrt{L_q^2\psi_f^2 + 8\left(L_d - L_q\right)^2\left(\frac{u_{\text{smax}}}{\omega_e}\right)^2}}{4\left(L_d - L_q\right)L_d}$.

By expressing i_d and i_q in terms of the saliency ratio ρ, we obtain:

$$\begin{cases} i_d = -\frac{\psi_f}{L_d} + \frac{-\rho\psi_f + \sqrt{\left(\rho\psi_f\right)^2 + 8(1-\rho)^2\left(\frac{u_{\text{smax}}}{\omega_e}\right)^2}}{4(1-\rho)L_d} = i_{ch} + \Delta i_d \\ i_q = \frac{\sqrt{\left(\frac{u_{\text{smax}}}{\omega_e}\right)^2 - L_d^2\Delta i_d^2}}{\rho L_d} \end{cases} \tag{8}$$

where $\Delta i_d = \frac{-\rho\psi_f + \sqrt{\left(\rho\psi_f\right)^2 + 8(1-\rho)^2\left(\frac{u_{\text{smax}}}{\omega_e}\right)^2}}{4(1-\rho)L_d}$.

As shown in Figure 2, let the target speed be ω_e^* and its intersection point with the MTPV curve be R. The slope k_R at point R is calculated by Equation (9) as follows:

$$k_R = \frac{di_q}{di_d} = \frac{2L_d^2\left(L_d - L_q\right)i_d + \psi_f L_d\left(2L_d - L_q\right)}{2\left(L_d - L_q\right)L_q^2 i_q} \tag{9}$$

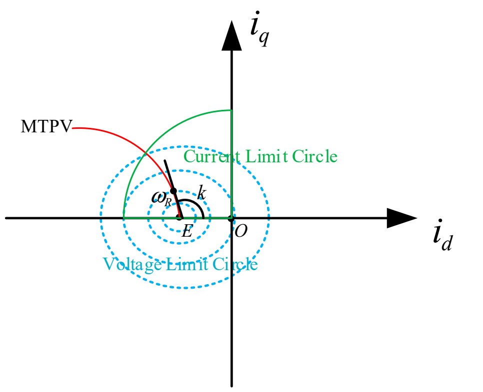

Figure 2. Schematic Diagram of the Speed-Point Tangency.

The d-axis current i_d is limited with a lower bound of $i_{dm} = -\psi_f / L_d$ and an upper bound of i_{dR} (the d-axis current at point R). Let Δi_d represent the difference between the current d-axis current i_d and its value at the previous time step, denoted as i_{d-last}. Then, the change in the q-axis current, Δi_q is given by Equation (10):

$$\Delta i_q = \frac{L_d\sqrt{\psi_f^2 + 4\left(L_d - L_q\right)^2 i_q^2}}{2L_q\left(L_d - L_q\right)i_q}\Delta i_d \tag{10}$$

Expressing this in terms of the slope yields:

$$\Delta i_q = k_R \Delta i_d \tag{11}$$

Therefore, the design procedure for the q-axis deep flux-weakening control strategy based on the MTPV principle is summarized as follows:

Step 1: Determine the critical condition of the d-axis current

Identify the critical d-axis current i_{dR} at the intersection point of the MTPV curve and the current limit circle. When the absolute value of i_d exceeds i_{dR}, the IPMSM enters the deep flux-weakening region.

Step 2: Track the MTPV trajectory in the deep flux-weakening region

Once the deep flux-weakening region is entered, the IPMSM operates along the MTPV trajectory for flux-weakening speed regulation, while the corresponding i_d value is obtained.

Step 3: Calculate the increment of the d-axis current

Based on the value of i_d obtained in Step 2, compute the increment Δi_d.

Step 4: Regulate the q-axis current

Using the increment Δi_d, calculate the change in the q-axis current Δi_q. Apply negative feedback to the q-axis current from the previous time step i_{q-last}, such that the current-time q-axis current becomes $i_q = i_{q-last} - \Delta i_q$, thereby completing the regulation of i_q.

3. Deep Flux-Weakening Control Strategy Based on an Adaptive RNN

Based on the research and analysis in Section 2.2, this study established that deep flux-weakening speed regulation of the IPMSM is achieved by adjusting the increments of the d- and q-axis currents, Δi_d and Δi_q, within the deep flux-weakening region. However, due to the strong coupling nature of the IPMSM, determining the appropriate values for Δi_d and Δi_q under large-disturbance operating conditions is highly complex. Direct calculation of these increments can lead to significant errors, which, during ultra-high-speed flux-weakening operation, can easily induce system oscillations. To mitigate this issue, this section builds upon the foundation laid in Section 2.2 by introducing a RNN strategy. Furthermore, the neural network model is optimized to ensure stable operation of the IPMSM within the deep flux-weakening region.

3.1. RNN Modeling

A Recurrent Neural Network is a type of neural network characterized by its short-term memory capability. As illustrated in Figure 3, a typical RNN consists of an input layer, a hidden layer, and an output layer, along with a time-delay feedback mechanism (delayer). In an RNN, neurons can receive information not only from other neurons but also from themselves through feedback loops, creating a cyclic network architecture. Compared to traditional feedforward neural networks, the structure of RNNs more closely resembles that of biological neural networks. The parameters of an RNN can be learned using the Backpropagation Through Time (BPTT) algorithm.

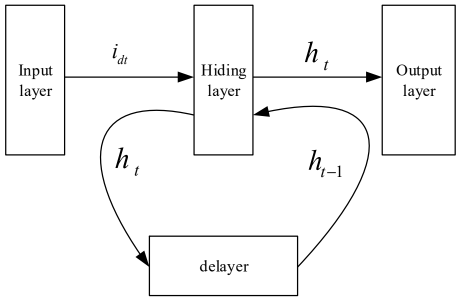

Figure 3. Schematic diagram of the RNN logic.

The logic for RNN-based deep flux-weakening control is illustrated in Figure 4. When $i_d > i_{dR}$, the IPMSM enters the deep flux-weakening region, triggering the RNN-based deep flux-weakening speed regulation strategy. This strategy requires sampling the d-axis current i_{dt-1} and the q-axis current i_{qt-1} from the previous time step, the current operating speed of the motor ω_fdk, and the target reference speed ω^*. These inputs are used to determine the current rate k_{Rt} and the d-axis current increment Δi_{dt}. After processing by the RNN, the network directly outputs the required d-axis current i_{dt} and q-axis current i_{qt} for the control system at the current time step. This approach significantly accelerates the response speed of the current loop in the deep flux-weakening region. Furthermore, the RNN inherently filters out significant disturbance points, thereby substantially enhancing the system's stability.

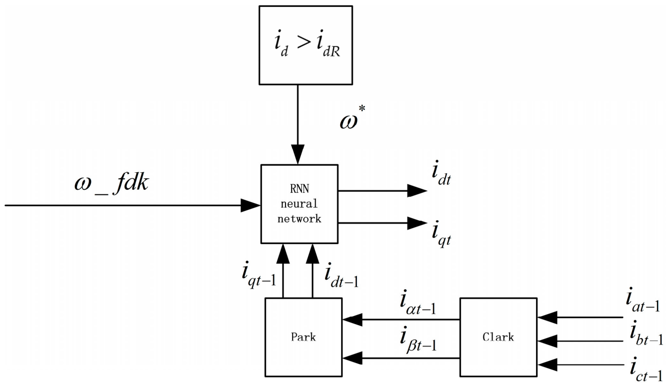

Figure 4. Block diagram of the RNN-based deep flux-weakening control logic.

Based on the preceding analysis, the MTPV-based deep flux-weakening control strategy is enhanced through integration with an RNN. The overall procedure is summarized in the following five steps:

Step 1: Condition Determination and Input Acquisition

First, determine whether the motor has entered the deep flux-weakening region using the analytical formulas derived in Section 2. Then, use i_{dt-1}, i_{qt-1}, ω_fdk, and ω^* as the input layer to the RNN.

Step 2: Nonlinear Autoregressive Model Establishment

Using the inputs collected in Step 1, establish a nonlinear autoregressive model for the outputs i_d and i_q.

Step 3: Parameter Learning via Real-Time Recurrent Learning

Employ the Real-Time Recurrent Learning (RTRL) algorithm to train the parameters of the nonlinear autoregressive model.

Step 4: Model Optimization

Optimize the model to avoid common issues such as gradient vanishing, gradient explosion, and overfitting.

Step 5: Output Generation

Output the final values i_{dt} and i_{qt}, thereby completing the improved RNN-based deep flux-weakening control strategy.

3.2. Nonlinear Autoregressive Model

First, a nonlinear autoregressive model for i_d and i_q is established. An Autoregressive Model (AR model) is a common type of time series model in statistics. It predicts the state at time t using the historical information of a variable y_t, and its expression is given by Equation (12):

$$y_t = \omega_0 + \sum_{k=1}^{K} \omega_k y_{t-k} + \varepsilon_t \tag{12}$$

where K is a hyperparameter, ω_0, ω_k are learnable parameters, and $\varepsilon_t \sim N(\sigma^2)$ is the noise at time t, whose variance is constant and independent of time. As shown in Equation (13), define x_t as the input matrix, r_t as the hidden state transition matrix, and y_t as the output matrix:

$$x_t = \begin{bmatrix} i_{dt-1} \\ i_{qt-1} \end{bmatrix}, r_t = \begin{bmatrix} \Delta i_{dt} \\ \Delta i_{qt} \end{bmatrix}, y_t = \begin{bmatrix} i_{dt} \\ i_{qt} \end{bmatrix} \tag{13}$$

The mathematical relationship between these matrices is given by Equation (14):

$$y_t = x_t + r_t \tag{14}$$

At each time step t, a set of external inputs x_t produces a corresponding output y_t. A delay unit records the most recent K_x external inputs and the most recent K_y outputs. The output y_t of the model at time t is given by Equation (15):

$$y_t = f\left(x_t, x_{t-1}, \cdots, x_{dt-K_x}, x_{qt}, x_{qt-1}, \cdots, x_{qt-K_y}\right) \tag{15}$$

Here, the function f can be designed in the form of a feedforward neural network. The logic of a feedforward neural network is illustrated in Figure 5.

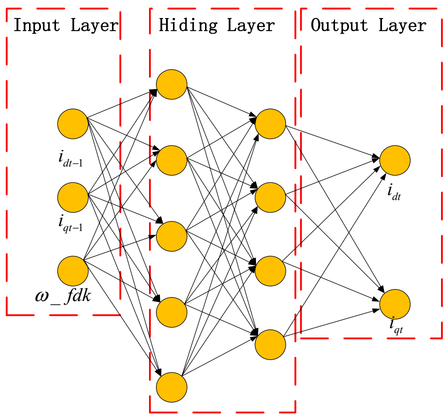

Figure 5. Logic diagram of the feedforward neural network.

Given an input sequence $i_{d:T} = (i_{d1}, i_{d2}, \cdots, i_{dt}, \cdots, i_{dT})$, the RNN updates the activation value h_t of its hidden layer with feedback connections according to Equation (16):

$$h_t = f(h_{t-1}, x_{dt}) \tag{16}$$

Here, $h_0 = 0$. Let the vector $x_t \in \mathbb{R}^M$ (denoting the input value of the d-axis current at time t) and $h_t \in \mathbb{R}^D$ (denoting the hidden state, i.e., the activation value of the hidden layer neurons). Since h_t depends not only on the current input x_t but also on the previous hidden state h_{t-1}, the update rule for the recurrent network at time t is given by Equation (17):

$$\begin{cases} z_t = Uh_{t-1} + Wx_t + b \\ h_t = g(z_t) \end{cases} \tag{17}$$

where Z_t is the net input of the hidden layer, $U \in \mathbb{R}^{D\times D}$ is the state-to-state weight matrix, $W \in \mathbb{R}^{D\times M}$ is the input-to-state weight matrix, $b \in \mathbb{R}^D$ is the bias vector, and $g(\bullet)$ is the Logistic activation function. Rewriting Equation (17) yields:

$$h_t = g(Uh_{t-1} + Wx_t + b) \tag{18}$$

Therefore, the control strategy of the RNN is given by Equation (19):

$$\begin{cases} h_t = f(h_{t-1}, x_t) \\ i_{qt} = o(h_t) \end{cases} \tag{19}$$

Equation (19) can be represented by a two-layer neural network, as given in Equation (20):

$$\begin{cases} h'_t = f(Ah_{t-1} + Bx_t + b) = f\left(ACh'_{t-1} + Bx_t + b\right) \\ h_t = Ch'_t \\ y'_t = f(A'h_{t-1} + B'x_t + b') = f\left(A'Ch'_{t-1} + Bx_t + b'\right) \\ y_t = Dy'_t \end{cases} \tag{20}$$

where A, B, C, A', B', C' are the weight matrices and b, b' are the bias vectors.

Rewriting Equation (20) in a structured form yields the layered RNN control strategy expressed by Equation (21):

$$\begin{cases} \begin{bmatrix} h'_t \\ y'_t \end{bmatrix} = f\left(\begin{bmatrix} AC & 0 \\ A'C & 0 \end{bmatrix}\begin{bmatrix} h'_{t-1} \\ y'_{t-1} \end{bmatrix} + \begin{bmatrix} B \\ B' \end{bmatrix} x_t + \begin{bmatrix} b \\ b' \end{bmatrix}\right) \\ y_t = \begin{bmatrix} 0 & D \end{bmatrix}\begin{bmatrix} h'_t \\ y'_t \end{bmatrix} \end{cases} \tag{21}$$

3.3. Parameter Learning

The RNN adopts a synchronous sequence mode for parameter learning, as illustrated in Figure 6. In this mode, for each time step t, a unique set of inputs x_t corresponds to a set of outputs y_t. Moreover, the input layer and the hidden layer at the current time step are both closely dependent on the parameter states from the previous time step.

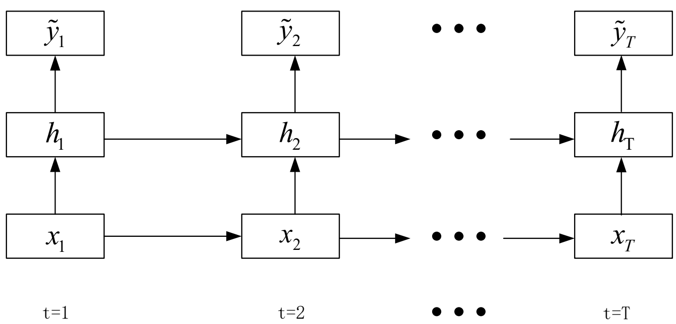

Figure 6. RNN synchronous sequence mode.

After establishing the regression model, the parameters of the RNN are learned via the gradient descent method. The collected data sequences x_T and their corresponding temporal labels are used as training samples (x_T, θ), where $x_{1:T} = (x_1, \cdots, x_T)$ is an input sequence of length T, and $\theta_{1:T} = (\theta_1, \cdots, \theta_T)$ is a label sequence of length T. This means that at each time step t, there is a corresponding supervisory signal θ_t.

The loss function at time t is defined by Equation (22):

$$\zeta_t = \zeta(\theta_t, g(h_t)) \tag{22}$$

where $g(h_t)$ is the output at time t, and ζ is a differentiable cross-entropy function. Therefore, the total loss function over the entire sequence is given by Equation (23):

$$\zeta_t = \sum_{t=1}^{T} \zeta_t \tag{23}$$

The gradient of the total sequence loss ζ with respect to the parameter U is the sum of the partial derivatives of the loss ζ_t at each time step with respect to U, as expressed by Equation (24):

$$\frac{\partial \zeta}{\partial U} = \sum_{t=1}^{T} \frac{\partial \zeta_t}{\partial U} \tag{24}$$

The Real-Time Recurrent Learning (RTRL) algorithm is employed to compute the gradients through forward propagation. Let the state of the model at time step $t+1$, denoted as h_{t+1}, be given by Equation (25):

$$h_{t+1} = f(z_{t+1}) = f(Uh_t + Wx_{t+1} + b) \tag{25}$$

Its partial derivative with respect to the parameter u_{ij} is given by Equation (26):

$$\frac{\partial h_{t+1}}{\partial u_{ij}} = \left(\frac{\partial^+ z_{t+1}}{\partial u_{ij}} + \frac{\partial h_t}{\partial u_{ij}} U^T \right) \frac{\partial h_{t+1}}{\partial z_{t+1}} = \left(\varphi_i \left([h_t]_j \right) + \frac{\partial h_t}{\partial u_{ij}} U^T \right) \odot \left(f'(z_{t+1}) \right)^T \tag{26}$$

The hidden state of the RNN is computed starting from time t_1. Based on Equation (26), the partial derivatives of the RNN are calculated in a forward manner. Assuming a supervisory signal exists at time t, with a corresponding loss function ζ_t, the partial derivative of the loss function with respect to u_{ij} is given by Equation (27):

$$\frac{\partial \zeta_t}{\partial u_{ij}} = \frac{\partial h_t}{\partial u_{ij}} \frac{\partial \zeta_t}{\partial h_t} \tag{27}$$

Based on Equation (27), the gradient of the loss function ζ_t with respect to the parameter U is computed in real-time at each moment t, and the parameter U is updated accordingly. The training procedures for the parameters W and b follow the same analytical method described above for U, thereby completing the parameter learning process for the RNN.

3.4. Optimization and Improvement of the RNN-Based Control Strategy

When using an RNN to control the deep flux-weakening operation of an IPMSM, the strategy is optimized to prevent the issues of vanishing or exploding gradients during the parameter learning process.

Let $U = I$ (the identity matrix), and let $\partial h_t / \partial h_{t-1}$ also be an identity matrix. Then, the relationship between h_t and h_{t-1} is given by Equation (28):

$$h_t = h_{t-1} + g(x_t, h_{t-1}; \theta) \tag{28}$$

From Equation (28), it can be observed that the relationship between the hidden states h_t and h_{t-1} encompasses both linear and nonlinear components. Introducing the nonlinear term can effectively alleviate the issue of vanishing gradients. To address the problem of exploding gradients in the recurrent neural network, a new internal state, denoted as c_t ($c_t \in \mathbb{R}^D$), is introduced based on Equation (28) to manage the linear recurrent information flow internally. Simultaneously, the nonlinear output information is passed to the external state h_t of the hidden layer. Setting $h_t \in \mathbb{R}^D$, the adjustment method for c_t is given by Equation (29):

$$\begin{cases} c_t = f_t \odot c_{t-1} + x_t \odot \widetilde{c}_t \\ h_t = o_t \odot \tanh(c_t) \end{cases} \tag{29}$$

where $f_t \in [0, 1]^D$, $i_t \in [0, 1]^D$, $o_t \in [0, 1]^D$. The vectors f_t, i_t, o_t represent three gates that control the path of information flow. The symbol $\odot$ denotes the element-wise product of vectors; c_{t-1} is the memory cell from the previous time step; $\widetilde{c}_t \in \mathbb{R}^D$ is the candidate state obtained through a nonlinear function. Combining these with Equation (29) yields the expression for c_t:

$$c_t = \tanh(W_c i_{dt} + U_c h_{t-1} + b_c) \tag{30}$$

The internal state c_t of the RNN records the historical information up to the current time step. This strategy introduces a gating mechanism to control the path of information flow. In Equation (30), the three gates are the input gate x_t, the forget gate f_t, and the output gate o_t. Their respective functions are as follows:

The forget gate f_t controls how much information from the previous internal state c_{t-1} is to be discarded (or forgotten).

The input gate x_t controls how much information from the current candidate state $\widetilde{c}_t$ is to be retained (or saved) in the new cell state.

The output gate o_t controls how much information from the current internal state c_t is output to the external state h_t.

When $f_t = 0$, $x_t = 1$, the memory cell is cleared of historical information, and the candidate state vector $\widetilde{c}_t$ is written into it. However, at this point, the memory cell c_t remains dependent on the historical information from the previous time step.

When $f_t = 1$, $x_t = 0$, the memory cell will cease to write new information and instead replicates the content from the previous time step. This mechanism controls the rate of information accumulation, allowing for the selective filtering and incorporation of new information, as well as the appropriate forgetting of previously accumulated historical data.

The values of the forget gate f_t, input gate x_t, and output gate o_t range between 0 and 1. These values function as scaling factors that regulate the proportion of information allowed to pass through each gate. Their calculation is defined by Equation (31):

$$\begin{cases} x_t = \sigma(W_i x_t + U_i h_{t-1} + b_i) \\ f_t = \sigma\left(W_f x_t + U_f h_{t-1} + b_f\right) \\ o_t = \sigma(W_o x_t + Uoh_{t-1} + b_o) \end{cases} \tag{31}$$

where $\sigma(\bullet)$ denotes the logistic function, whose output range is (0, 1). Here, x_t represents the input parameters to the RNN at the current time step, and h_{t-1} denotes the output parameters of the control strategy from the previous time step.

The structure of the optimized RNN recurrent unit is shown in Figure 7. The following steps primarily describe the operations within its hidden layer:

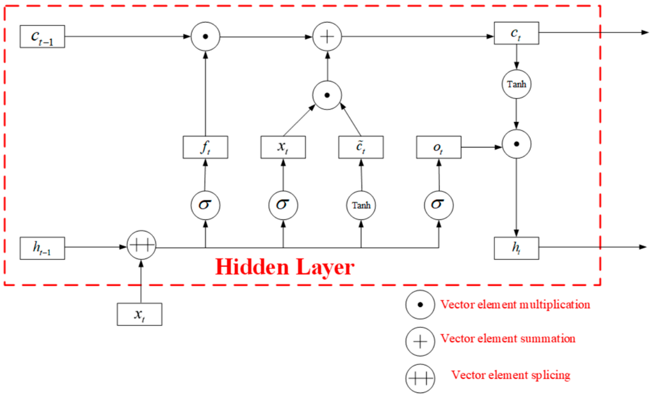

Figure 7. Optimized recurrent unit structure of the RNN.

Step 1: Calculate Gates and Candidate State

Using the external state from the previous time step, h_{t-1}, and the input at the current time step, x_t, calculate the three gates and the candidate state $\widetilde{c}_t$.

Step 2: Update Memory Cell

Update the memory cell c_t by combining the effects of the forget gate f_t and the input gate x_t.

Step 3: Compute External State

Using the output gate o_t, transfer information from the internal state to the new external state h_t.

Through the aforementioned improvement and optimization strategies, the overall RNN architecture can establish long-term temporal dependencies. By combining Equations (29)–(31), the optimized strategy can be concisely described by Equation (32):

$$\begin{cases} \begin{bmatrix} c_t \\ o_t \\ x_t \\ f_t \end{bmatrix} = \begin{bmatrix} \tanh \\ \sigma \\ \sigma \\ \sigma \end{bmatrix} \left(W \begin{bmatrix} x_t \\ h_{t-1} \end{bmatrix} + b \right) \\ c_t = f_t \odot c_{t-1} + x_t \odot \widetilde{c}_t \\ h_t = o_t \odot \tanh(c_t) \end{cases} \quad (32)$$

The adaptive RNN deep flux-weakening controller proposed in this paper is implemented based on a Long Short-Term Memory (LSTM) network, with its network architecture shown in Figure 7. Training employs the Adam optimizer, and key hyperparameter configurations are listed in Table 1. The network convergence process exhibits a characteristic three-phase progression (as shown in Figure 7): during the rapid descent phase (cycles 1–10), the loss value quickly dropped from 1.247 to 0.186, indicating that the network rapidly learned the basic mapping of current commands; in the steady convergence phase (cycles 11–40), the learning rate decayed to 0.0005 by cycle 20, the loss further decreased to 0.053, and the validation loss declined synchronously with the training loss, showing no signs of overfitting; during the stable plateau phase (cycles 41–60), the loss finally converged to 0.037, with the validation loss stabilizing at 0.041. The gap between them remained within 10.8%, demonstrating excellent generalization capability of the model. To enhance robustness, Dropout rates of 0.3 and 0.2 were applied after the LSTM layer and the fully connected layer, respectively, to mitigate overfitting. Meanwhile, gradient norms were effectively constrained below the threshold of 1.0 throughout the training process, preventing gradient explosion and ensuring training stability.

Table 1. RNN hyperparameters.

Hyperparameters	Value
Number of training cycles	60
Batch size	256
Initial learning rate	0.001
Learning rate scheduling	Decreases by half every 20 cycles
Gradient threshold	1.0
Dropout rate	0.3/0.2
Validation set proportion	15%

The training of the optimized RNN essentially relies on its gating mechanism to dynamically manage internal states across time, fundamentally overcoming the inherent issues of traditional simple RNNs during training. Although the training process still follows the framework of backpropagation through time (BPTT), as gradients flow through the specially designed "constant error carousel"—i.e., the cell state—the multiplicative terms remain within a reasonable range, effectively circumventing the problems of vanishing or exploding gradients. This enables the network to learn long-term dependencies spanning hundreds or even thousands of time steps.

During training, the network achieves fine-grained regulation of information flow through the coordinated operation of the input gate, forget gate, and output gate. The hidden state is no longer passively overwritten; instead, based on the current input and historical state, it actively chooses to retain critical information and discard non-essential content. This mechanism not only makes model training more stable and efficient but also endows its internal states with the ability to maintain long-term memory of key events in sequences while effectively filtering out noise.

Thanks to these structural innovations, the improved RNN can proactively and selectively manage information flow, effectively identifying and remembering key contextual information in long sequences, thereby significantly enhancing its ability to model long-term dependencies. This advancement has enabled the model to demonstrate outstanding robustness and accuracy in complex sequence modeling tasks that require deep contextual understanding, such as machine translation and text generation, further propelling RNN from a theoretical model toward widespread industrial-grade applications.

4. Simulation Results and Analysis

To validate the effectiveness of the proposed adaptive RNN algorithm for deep flux-weakening control, a series of simulations were conducted in MATLABR2024b/Simulink. The simulation parameters are listed in Table 2. The block diagram of the control system based on the adaptive RNN is shown in Figure 8 below. The parameters of the PI controllers are set as follows: the speed PI controller has a proportional gain K_P of 5 and an integral gain K_I of 0.05; the d-axis PI controller is configured with $K_P = 40$ and $K_I = 60$; and the q-axis PI controller uses $K_P = 20$ and $K_I = 60$. Using the d-axis deep flux-weakening formula method provided in Section 2, a training dataset was generated via simulation in MATLAB. The adaptive RNN was then employed to perform the deep flux-weakening control, replacing the formula-based method. The maximum current vector magnitude I_{smax} was set to 120 A, with the d-axis inductance $L_d =$ 0.2 mH and the q-axis inductance $L_q =$ 0.4 mH. The fitted MTPV curve is illustrated in Figure 9.

Table 2. Parameters of the IPMSM simulation model.

Parameter Name	Value
n_{max} [rpm]	5000
T_{emax} [Nm]	40
p_n	4
J [kgm^2]	0.01
R [Ω]	0.025
ψ_f [Wb]	0.062
L_d [H]	0.0002
L_q [H]	0.0004

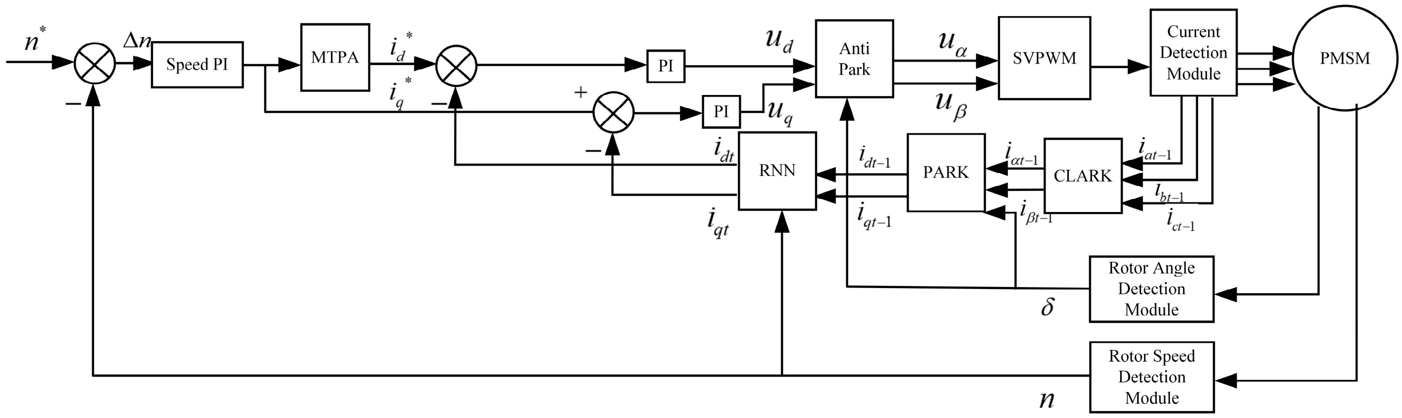

Figure 8. Control block diagram of the system based on the adaptive RNN.

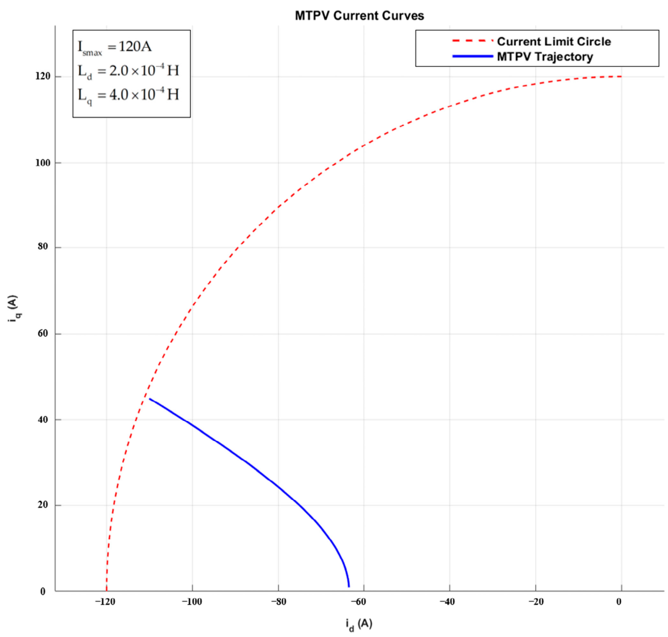

Figure 9. MTPV trajectory fitting curve of the adaptive RNN.

4.1. Speed Response Comparison

Upon entering the deep flux-weakening region, the voltage stabilizes at the maximum value of the bus voltage vector, u_{smax}. The bus voltage specified in the simulation model is 192 V. Since the system employs SVPWM modulation, a voltage vector anti-saturation coefficient $k = 0.9$ is introduced to prevent saturation of the current regulator once the operating point approaches the saturation limit. Consequently, the tuned value of u_{smax} should be:

$$u_{\text{smax}} = k\frac{u_{dc}}{\sqrt{3}} = 0.9 \times \frac{192}{\sqrt{3}} = 99.7 \text{ V} \tag{33}$$

Under no-load conditions at a given speed of 5000 r/min, the startup acceleration performance of the traditional flux-weakening control strategy, the fuzzy logic control strategy, and the RNN flux-weakening control strategy is compared in Figure 10. Quantitative analysis shows that with the RNN flux-weakening control strategy, the IPMSM reaches the target speed in 0.162 s, whereas the traditional method and the fuzzy logic method require 0.190 s and 0.189 s, respectively. This represents a significant reduction in response time of approximately 14.7%. These results verify that the adaptive RNN control effectively enhances the system's dynamic response capability through online real-time tuning of control parameters. Its acceleration process is faster and demonstrates superior speed-tracking performance.

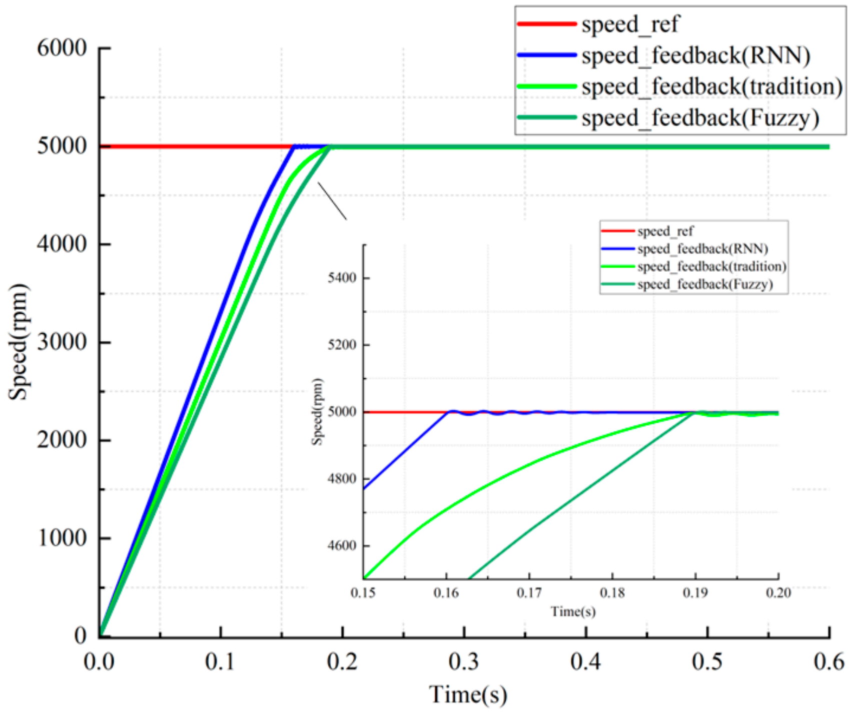

Figure 10. Speed waveforms during no-load startup based on RNN flux-weakening control, traditional flux-weakening control and Fuzzy Logic Flux-Weakening Strategy methods.

4.2. Steady-State Performance Validation

To evaluate the steady-state performance of the control system in the high-speed region, a comparative experiment was conducted on the operational characteristics of the IPMSM under a no-load steady-state condition at 5000 r/min, using the adaptive RNN flux-weakening control strategy, the traditional flux-weakening control strategy, and the fuzzy logic flux-weakening strategy. The results are shown in Figure 11. The simulation results indicate that, compared with the traditional flux-weakening control method, the RNN-based control strategy demonstrates superior overall performance in steady-state operation, achieving steady-state error-free speed tracking. When compared with the fuzzy logic flux-weakening strategy, the RNN strategy shows a slight advantage in terms of torque ripple coefficient and total current harmonic distortion rate. These results verify that the proposed adaptive RNN flux-weakening control strategy possesses online dynamic adjustment capabilities, effectively compensating for variations in motor parameters and nonlinear effects. Consequently, it enhances both the steady-state control accuracy and operational smoothness of the system in the deep flux-weakening high-speed range.

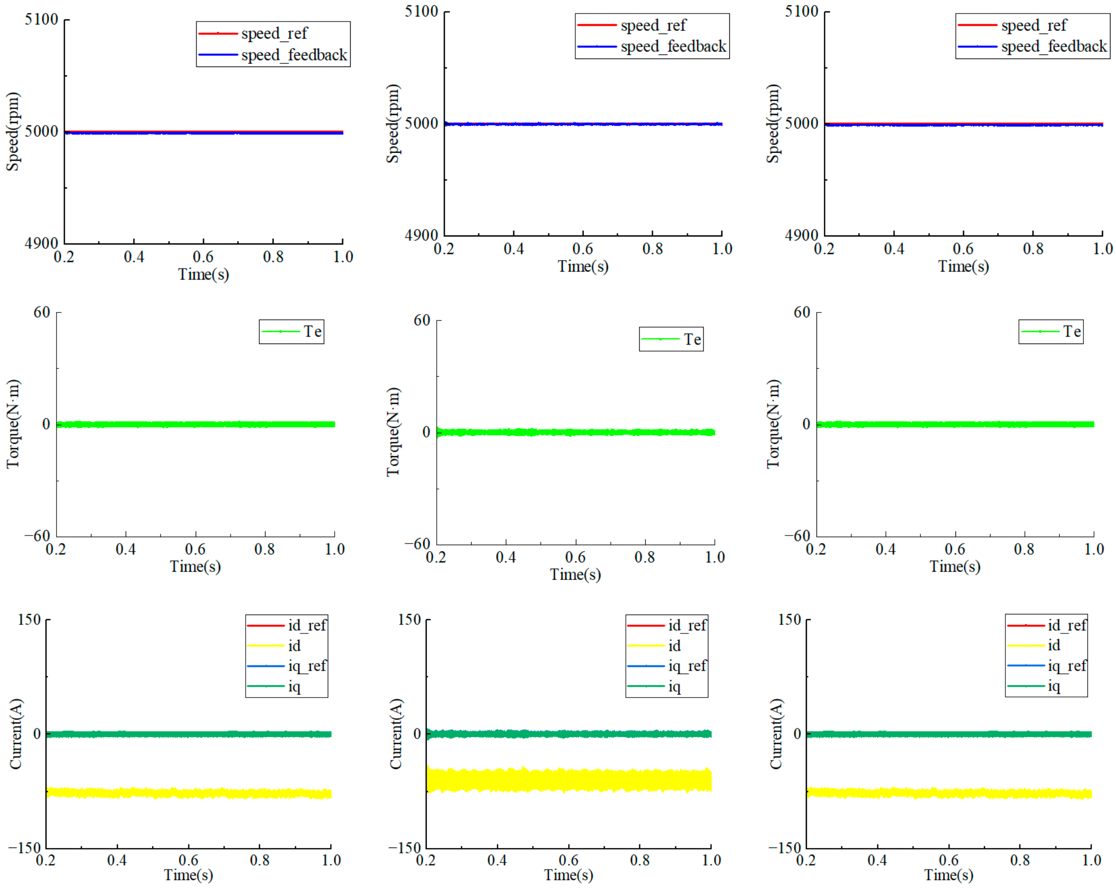

(**a**) (**b**) (**c**)

Figure 11. Waveform comparison during no-load startup at a given speed of 5000 r/min: (**a**) RNN-based flux-weakening strategy (**b**) traditional flux-weakening strategy (**c**) Fuzzy Logic Flux-Weakening Strategy.

4.3. Dynamic Performance Validation

To comprehensively evaluate the dynamic performance and disturbance-rejection robustness of the control system in the high-speed region, this paper designed and conducted three sets of comparative simulation experiments.

The first experiment aimed to verify the controller's robustness against stator resistance parameter perturbation. Under a steady-state no-load condition at 5000 r/min, the stator resistance value in the motor model was instantaneously increased to 150% of its nominal value to simulate extreme temperature rise effects. The dynamic responses of key system variables, including speed, electromagnetic torque, and d-q axis currents, are shown in Figure 12.

The second experiment focused on examining the controller's adaptability to inductance parameter saturation effects. Starting under a load of 10 Nm at 5000 r/min, the d-axis and q-axis inductance values were synchronously reduced to 70% of their nominal values after the system reached steady state, simulating the high-current magnetic saturation phenomenon in the deep flux-weakening region. The dynamic response curves of the system under this condition are presented in Figure 13.

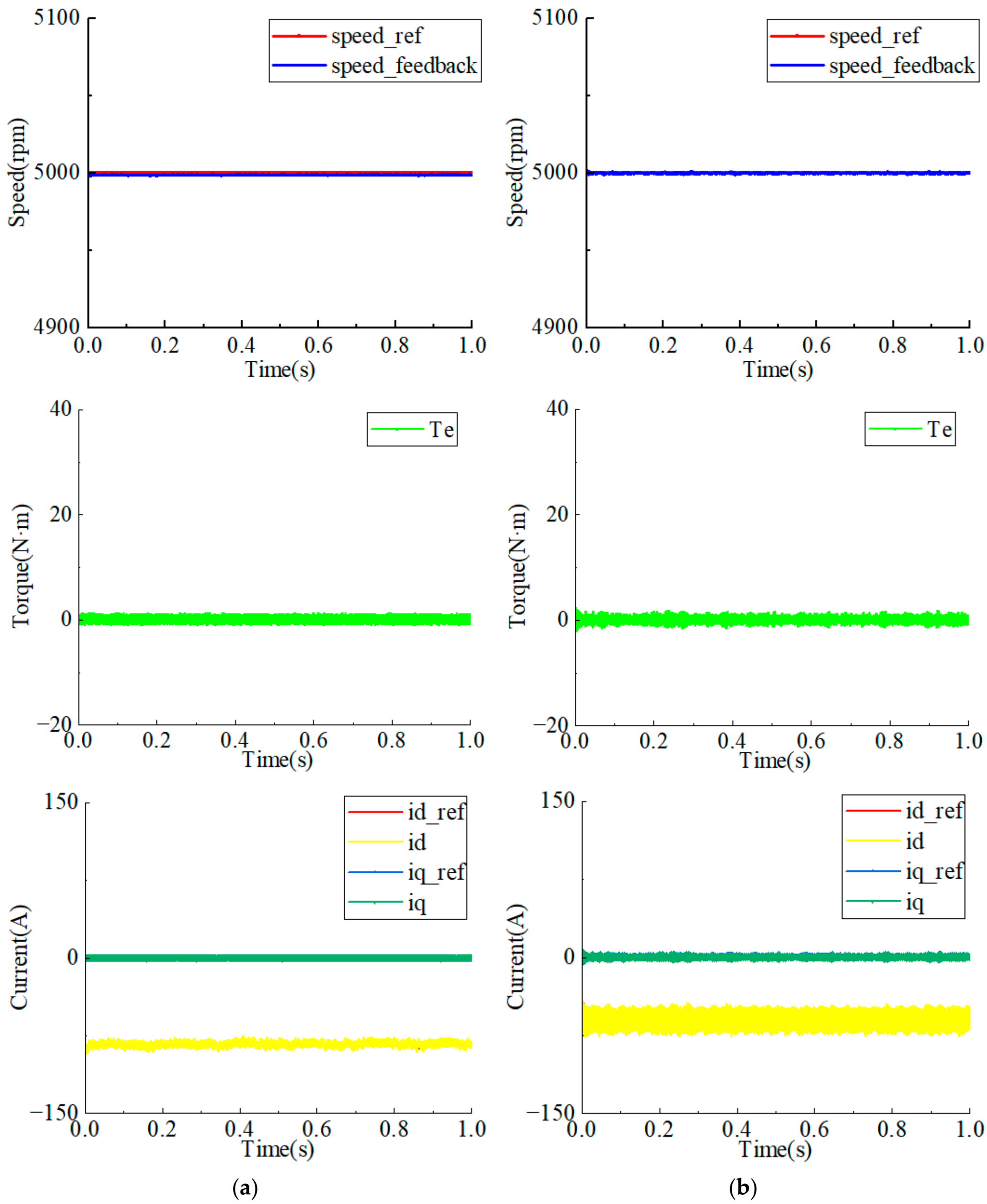

Figure 12. Waveform Comparison of Speed, Torque, and Current When Stator Resistance is Increased to 150%: (**a**) RNN Flux-Weakening Strategy (**b**) Traditional Flux-Weakening Strategy.

The third experiment was a load disturbance test designed to compare the dynamic disturbance rejection performance of the proposed adaptive RNN flux-weakening control against the traditional method. Under a steady-state no-load condition at 5000 r/min, a step load disturbance with an amplitude of 10 Nm was applied to both control systems: instantaneously loaded at 0.2 s and removed at 0.8 s. The comparative results of the dynamic response waveforms for speed, electromagnetic torque, and d-q axis currents under the two control strategies are shown in Figure 14.

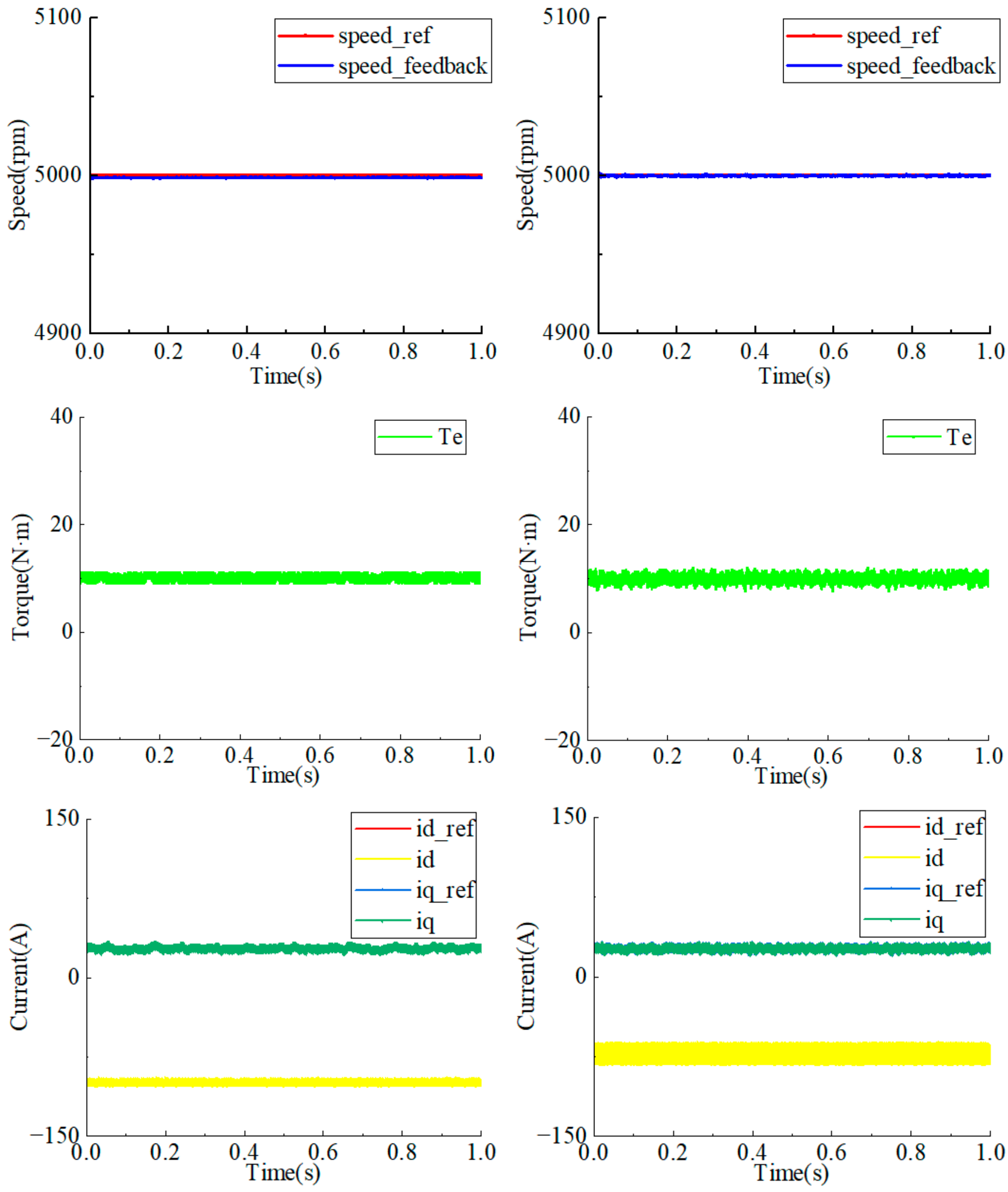

Figure 13. Waveform Comparison of Speed, Torque, and Current When d-axis and q-axis Inductances Decrease to 70%: (**a**) RNN Flux-Weakening Strategy (**b**) Traditional Flux-Weakening Strategy.

The simulation results indicate that both control strategies can achieve fundamental regulation of speed and torque during internal parameter variations and sudden load changes, and the current loops also demonstrate certain dynamic response capabilities. However, significant differences exist in dynamic performance metrics: the traditional flux-weakening strategy exhibits more pronounced speed fluctuation and a slower recovery process upon sudden loading, whereas the RNN flux-weakening strategy demonstrates stronger disturbance suppression capability, with smaller dynamic speed drop and faster recovery. Specifically, under the RNN strategy, the dynamic speed drop rate and speed recovery time are approximately 0.24% and 0.014 s, respectively, significantly outperforming the 1% and 0.048 s of the traditional strategy. Furthermore, the waveforms of electromagnetic torque and d-q axis currents under RNN control show smaller fluctuations and more stable, rapid responses. To systematically quantify and evaluate the dynamic performance, key metrics such as speed settling time, overshoot, dynamic speed drop rate, and recovery time are summarized in Table 3.

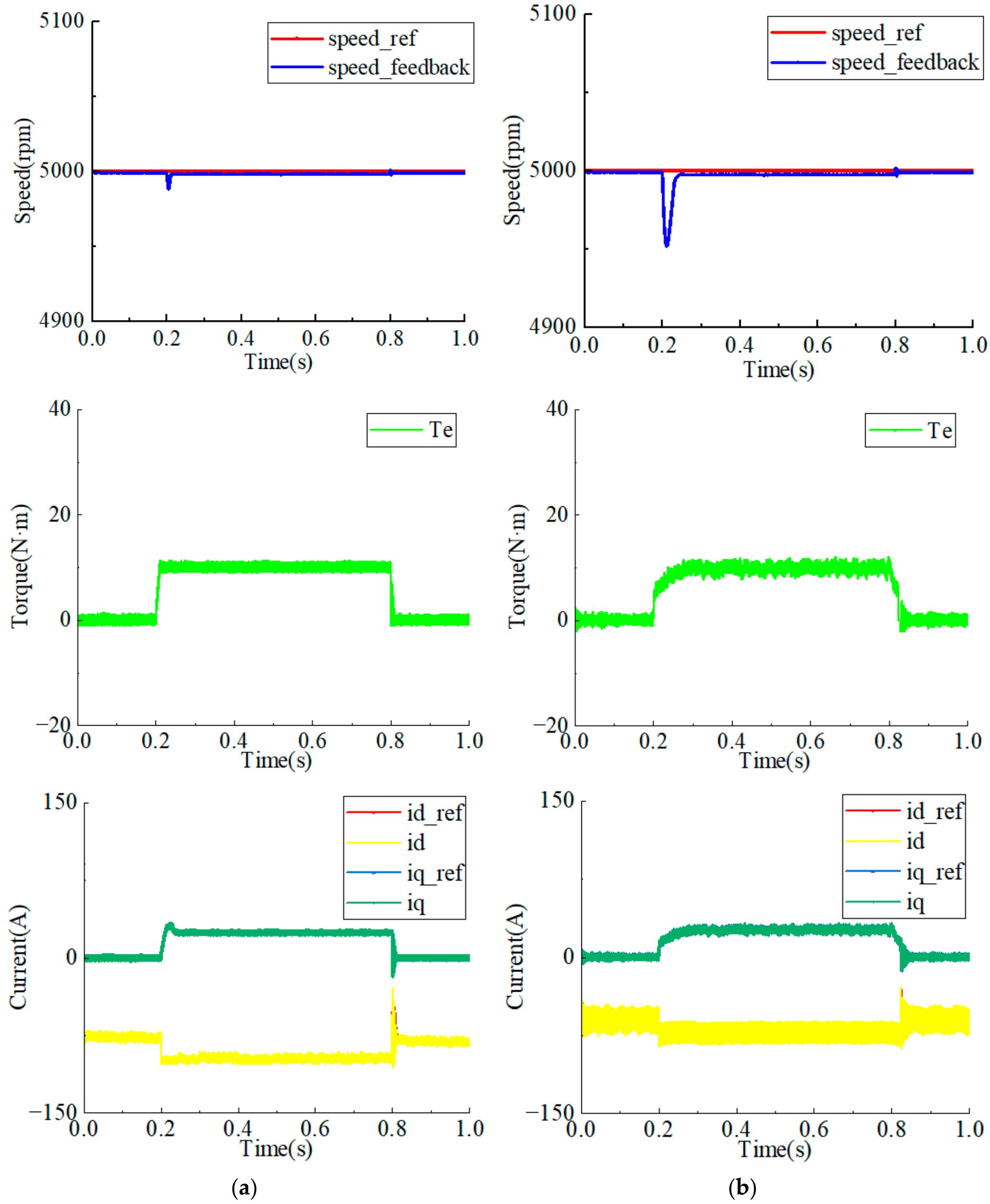

Figure 14. Comparison of speed, torque, and current waveforms under a 10 Nm load disturbance: (**a**) RNN-based flux-weakening strategy (**b**) traditional flux-weakening strategy.

Table 3. Quantitative Analysis of Dynamic Performance.

Control Strategy	RNN Weak Magnetic Strategy	Traditional Weak Magnetic Strategy
Settling time [s]	0.162	0.190
Overshoot [%]	0.24	0.30
Dynamic speed drop [%]	0.24	1
Recovery time [s]	0.014	0.048

4.4. Robustness Analysis

To further quantitatively evaluate the performance of the control strategies, this paper conducted a comprehensive comparison among the traditional flux-weakening strategy, the fuzzy logic strategy, and the proposed adaptive RNN flux-weakening strategy across three dimensions: dynamic response, steady-state quality, and system efficiency. The results are summarized in Table 4. Data analysis indicates that the adaptive RNN strategy demonstrates significant advantages in all key metrics: In terms of dynamic performance, its speed settling time (0.162 s) is reduced by 14.7% and 14.3% compared to the traditional strategy (0.190 s) and the fuzzy logic strategy (0.189 s), respectively. Regarding steady-state performance, it achieves the lowest torque ripple (1.2%) and total current harmonic distortion (3.1%). In energy efficiency, the overall system efficiency reaches 96.8%, surpassing the 91.8% of the traditional strategy and the 95.9% of the fuzzy logic strategy.

Table 4. Comparative performance table.

Control Strategy	RNN Weak Magnetic Strategy	Traditional Weak Magnetic Strategy	Fuzzy Logic Flux-Weakening Strategy
Settling time [s]	0.162	0.190	0.189
Torque ripple coefficient (steady-state ripple) [%]	1.2	1.8	1.4
Total Current Harmonic Distortion Rate (Steady-state Ripple) [%]	3.1	4.5	3.3
Energy efficiency [%]	96.8	91.8	95.9

Integrating the simulation results from this chapter, a comparison among the traditional, fuzzy logic, and adaptive RNN flux-weakening strategies is conducted from the perspectives of dynamic tracking, steady-state quality, and robustness. The simulation results show that: In dynamic performance, the RNN strategy achieves the fastest speed response, improving by approximately 14% compared to the other two strategies. In steady-state performance, it exhibits the lowest current harmonic distortion and torque ripple, indicating the highest control accuracy. In robustness, when facing parameter variations and sudden load changes, the dynamic speed drop and recovery time of the RNN strategy are significantly superior to those of the traditional strategy.

The experiments consistently demonstrate that the proposed adaptive RNN strategy holds significant advantages in dynamic response, steady-state accuracy, and disturbance-rejection robustness, validating its advanced and effective performance under high-speed deep flux-weakening conditions.

5. Conclusions

This paper proposes an intelligent control algorithm based on an adaptive RNN. By formulating a constrained optimization problem, the deep flux-weakening control of the IPMSM is effectively integrated with the structure of the RNN, thereby addressing the challenges of complex parameter tuning and reliance on accurate motor models in traditional flux-weakening methods. To further enhance control performance, the RNN structure was optimized to improve its capability in modeling long-term temporal dependencies during dynamic processes, which significantly increased the accuracy of parameter tuning and the robustness of control.

The simulation results indicate that the adaptive RNN-based flux-weakening control strategy proposed in this paper demonstrates high accuracy in parameter calculation and rapid system response. Under various operating conditions, including no-load startup, high-speed steady-state operation, internal parameter variations, and sudden load changes, the strategy consistently exhibits excellent dynamic and static performance. Specifically, in terms of speed response, the RNN strategy reduced the time required to accelerate the motor to 5000 r/min from 0.190 s (with the traditional method) to 0.162 s, improving the dynamic response speed by approximately 14.7%. In terms of steady-state performance, the RNN-based flux-weakening control strategy achieves steady-state error-free tracking of rotational speed, demonstrates effective decoupling of the d-q axis currents, and significantly reduces torque ripple, with the dynamic speed drop rate decreasing from 1% to 0.24%. In terms of disturbance rejection performance, the proposed RNN-based flux-weakening control strategy demonstrates excellent performance under various disturbance conditions. It maintains stable operation even when internal motor parameters undergo perturbations, highlighting its strong parameter robustness. Particularly in the dynamic step-load test, this strategy significantly reduces the speed recovery time from 0.048 s with the traditional method to 0.014 s—a reduction of 70.8%—underscoring its superior disturbance suppression capability and faster dynamic recovery characteristics.

In summary, the adaptive RNN-based flux-weakening control strategy proposed in this paper demonstrates significant feasibility and engineering advantages in the deep flux-weakening speed regulation region of IPMSMs. It not only effectively enhances the system's dynamic response speed and steady-state accuracy but also strengthens its adaptability and robustness across the full operating range. Simulation studies confirm that the strategy exhibits superior performance when coping with parameter variations and complex disturbances. However, it must be pointed out that before deep learning-based control methods can advance toward practical engineering applications, further research and verification are still required in areas such as computational efficiency for real-time deployment, theoretical guarantees of stability, and generalization capability under untrained operating conditions. Future work will focus on the following two directions: first, developing lightweight network architectures and hybrid control frameworks to achieve a better balance between control performance and engineering practicality; second, striving to construct an intelligent integrated control strategy for IPMSMs that covers the full operating range, enabling smooth and high-dynamic performance speed regulation from zero speed to the high-speed deep flux-weakening region.

Author Contributions: Conceptualization, Z.Y. and W.Z.; methodology, Z.Y. and W.Z.; validation, Z.Y. and P.Z.; writing—original draft preparation, Z.Y.; writing—review and editing, W.Z. and P.Z.; supervision, W.Z. and P.Z. All authors have read and agreed to the published version of the manuscript.

Funding: This research was supported by the Natural Science Foundation of Jiangsu Province No. BK20231257.

Data Availability Statement: The data presented in this study are available on request from the corresponding authors.

Conflicts of Interest: The authors declare no conflicts of interest.

References

1. Yao, K.; Du, B.; Li, J.; Huang, W.; Cheng, Y.; Zhang, Q.; Cui, S. Torque Closed-Loop Flux-Weakening Control of IPMSM Based on Search Coils. *IEEE Trans. Ind. Electron.* **2024**, *72*, 122–133. [CrossRef]
2. Wang, L.; Yu, Y.; Wang, B.; Xu, D. Power-Model-Based Adaptive Overmodulation Scheme for Field-Weakening Control of PMSM. *IEEE Trans. Ind. Electron.* **2024**, *71*, 11898–11909. [CrossRef]
3. Desai, J.P. Analytical Review of MTPA with Field Weakening Control of IPMSM on FEA Validated Design. *Trans. Indian Natl. Acad. Eng.* **2023**, *8*, 305–316. [CrossRef]
4. Zhang, Y.; Qi, R. Flux-weakening drive for IPMSM based on model predictive control. *Energies* **2022**, *15*, 2543. [CrossRef]
5. Chen, Z.; Jin, S.; Shen, Y.; Ma, Y.; Mao, X.; Shi, T. Maximum efficiency per torque control of IPMSM based on loss criterion acquisition. *IEEE Trans. Power Electron.* **2024**, *39*, 14107–14117. [CrossRef]

6. Gierczynski, M.; Niewiara, L.J.; Jakubowski, R.; Seredynski, M.; Jaworski, M.; Kupiec, E.; Grzesiak, L.M. Torque Control of a Highly-Saturated IPMSM Drive Using the Flux Linkage Control Scheme and an Augmented-State-Feedback Controller. *IEEE Trans. Ind. Electron.* **2025**, *72*, 10962–10973. [CrossRef]
7. Deng, W.; Zhang, Q.; Yan, B.; Li, S. Direct Torque Control of PMSM Drives for Common-Mode Voltage Reduction and Steady State Performance Improvement. *IEEE Trans. Transp. Electrif.* **2024**, *11*, 1629–1639. [CrossRef]
8. Wang, Y.; Zhang, Y.; Yang, H.; Rodriguez, J. Variable-vector-based model predictive control with reduced current harmonic and controllable switching frequency for PMSM drives. *IEEE Trans. Power Electron.* **2024**, *39*, 16429–16441. [CrossRef]
9. Monadi, M.; Nabipour, M.; Akbari-Behbahani, F.; Pouresmaeil, E. Speed control techniques for permanent magnet synchronous motors in electric vehicle applications towards sustainable energy mobility: A review. *IEEE Access* **2024**, *12*, 119615–119632. [CrossRef]
10. Wang, L.; Yu, Y.; Wang, B.; Xu, D. Bandwidth-Based Tuning Method for PMSM Field-Weakening Control with Speed Adaptation. *IEEE Trans. Ind. Electron.* **2025**, *72*, 10986–10997. [CrossRef]
11. Wu, J.; Liu, J.; Xie, C.; Guo, Z. Fuzzy Single-Current Field Weakening Control of IPMSM in EV. *Eng. Lett.* **2024**, *32*, 244.
12. Dianov, A. Improved Field-Weakening Control of PM Motors for Home Appliances Excluding Speed Loop Windup. *IEEE/ASME Trans. Mechatron.* **2025**, 1–10. [CrossRef]
13. Wang, L.; Yu, Y.; Dong, Q.; Xu, D. Direct Look-Up Table Method for Field-Weakening Control of Permanent Magnet Synchronous Motor Based on Operation Conditions. In Proceedings of the 2024 IEEE 7th International Electrical and Energy Conference (CIEEC), Harbin, China, 10–12 May 2024.
14. Zhou, Z.; Li, J.; Lu, Y.; Xu, H.; Zhang, Q.; Wu, L. Field Weakening Strategy Extended to Six-Step Operation for Dual Close-loop Current Control of Induction Motors. *IEEE Trans. Transp. Electrif.* **2024**, *11*, 2674–2683. [CrossRef]
15. Chen, Q.; Chen, J.; Shi, H.; Fu, L.; Liu, G. Flux Weakening Control of Dual Five-Phase Hybrid Excitation Permanent Magnet Synchronous Motor. *IEEE Trans. Transp. Electrif.* **2025**, *11*, 10415–10426. [CrossRef]
16. Iwama, K.; Hiyoshi, Y.; Noguchi, T. Dual Inverter Fed Adjustable Field IPMSM Using DC Zero-Sequence Current. *IEEE Trans. Ind. Electron.* **2024**, *72*, 3381–3391. [CrossRef]
17. Cheng, S.; Zou, J.; Zhang, W.; Xu, Y.; Zou, J. Research on Nonlinear Observer Sensorless Algorithm Based on Parameter Identification Under Field Weakening Control for SPMSMs. In Proceedings of the 2024 IEEE 7th International Electrical and Energy Conference (CIEEC), Harbin, China, 10–12 May 2024.
18. Zhang, L.; Zhang, M.; Zhu, X.; Pei, Z.; Chen, X. Space Decoupling Sensorless Control of Five-Phase Flux-Intensifying PM Motor Based on AFCCF-SMO Considering Flux-Weakening Operation. *IEEE Trans. Ind. Electron.* **2025**, *72*, 6865–6875. [CrossRef]
19. Zhao, W.; Li, L.; Wang, B.; Zhu, G.; Wang, N.; Wang, X. Improved Leading-Angle Flux-Weakening Control for Surface-Inset Permanent Magnet Synchronous Motor Considering Asymmetric Rotor Effects. *IEEE Trans. Power Electron.* **2025**, *40*, 9699–9708. [CrossRef]
20. Elhaj, A.; Alzayed, M.; Chaoui, H. Direct voltage MTPA control of interior permanent magnet synchronous motor driven electric vehicles. *Control. Eng. Pract.* **2025**, *156*, 106197. [CrossRef]
21. Jin, S.; Jin, W.; Wang, H.; Yu, S.; Zhang, Z. Maximum torque per ampere control of permanent magnet reluctance hybrid rotor dual stator synchronous motor based on sliding mode speed controller. *IET Power Electron.* **2024**, *17*, 2072–2082. [CrossRef]
22. Fan, Y.; Ma, H.; Zhu, G.; Luo, J. Improved MTPA and MTPV Optimal Criteria Analysis Based on IPMSM Nonlinear Flux-Linkage Model. *Energies* **2024**, *17*, 3494. [CrossRef]
23. Yang, J.; Xie, J.; Zhou, J.; Pang, H.; Wang, Y.; Liang, T. Initial Position Detection Strategy for PMSM Based on Improved Gradient Descent Algorithm and Elliptical Excitation Voltage Injection. In Proceedings of the 2024 5th International Conference on Mechatronics Technology and Intelligent Manufacturing (ICMTIM), Nanjing, China, 26–28 April 2024.
24. Canseven, H.T.; Petrov, I.; Pyrhönen, J. Impact of Stator Core Magnetic Asymmetry on the Properties of a High Specific Power PMSM. *IEEE Trans. Ind. Appl.* **2024**, *60*, 3830–3839. [CrossRef]
25. Kadupu, S.C.; Vaishnav, K.; Pandey, N.; Kant, P. Modified MTPA Controlled Interior Permanent Magnet Synchronous Motor Drive for Electric Vehicle Application Considering Magnetic Saturation. In Proceedings of the 2024 IEEE International Conference on Power Electronics, Drives and Energy Systems (PEDES), Mangalore, India, 18–21 December 2024.
26. Yu, W.; Qi, J.; Hua, W.; Zhou, J. Investigation of Interior Permanent Magnet Machine with Integrated High and Low Voltage Windings for Electronic Hydraulic Power Steering. *IEEE Trans. Transp. Electrif.* **2025**, *11*, 10378–10390. [CrossRef]
27. Wang, F.; Kong, W.; Wang, Z. Dynamic Flux Weakening-Based DPCC for Rapid Torque Rise of SPMSM Drives at Medium-to-High Speeds. *IEEE Trans. Ind. Electron.* **2025**, *72*, 11035–11047. [CrossRef]
28. Liu, D.; Han, J.; Chen, G.; Cheng, Y.; Liang, X.; Song, C. Fuzzy self-tuning fractional order PD permanent magnet synchronous motor speed control based on torque compensation. *Sci. Rep.* **2025**, *15*, 2141. [CrossRef] [PubMed]
29. Yu, J.; Li, S. Permanent magnet synchronous motor adaptive fractional order Fast terminal sliding mode control. In Proceedings of the 2024 36th Chinese Control and Decision Conference (CCDC), Xi'an, China, 25–27 May 2024.

30. Ma, Z.; Zhang, H.; Liu, J. DB-RNN: An RNN for Precipitation Nowcasting Deblurring. *IEEE J. Sel. Top. Appl. Earth Obs. Remote Sens.* **2024**, *17*, 5026–5041. [CrossRef]
31. Wu, T.; Zhu, H.; Wu, X.; Huang, S.; Yu, X.; Tan, Z.; Gao, F.; Tong, X. Enhanced Sequential High-Frequency Voltage Injection Method for Low-Speed Sensorless Control of IPMSM. *IEEE Trans. Power Electron.* **2025**, *40*, 10836–10845. [CrossRef]
32. Atashin, S.A.; Zarchi, H.A.; Markadeh, G.A. Online adaptive current vector adjustment for deep flux-weakening control of IPMSM. *IEEE Trans. Power Electron.* **2022**, *38*, 2339–2350. [CrossRef]

Disclaimer/Publisher's Note: The statements, opinions and data contained in all publications are solely those of the individual author(s) and contributor(s) and not of MDPI and/or the editor(s). MDPI and/or the editor(s) disclaim responsibility for any injury to people or property resulting from any ideas, methods, instructions or products referred to in the content.